

# Greatly Enhanced Emission from Spin Defects in Hexagonal Boron Nitride Enabled by a Low-Loss Plasmonic Nanocavity

Xiaohui Xu, Abhishek B. Solanki, Demid Sychev, Xingyu Gao, Samuel Peana, Aleksandr S. Baburin, Karthik Pagadala, Zachariah O. Martin, Sarah N. Chowdhury, Yong P. Chen, Takashi Taniguchi, Kenji Watanabe, Ilya A. Rodionov, Alexander V. Kildishev, Tongcang Li, Pramey Upadhyaya, Alexandra Boltasseva, and Vladimir M. Shalaev\*



Cite This: *Nano Lett.* 2023, 23, 25–33



Read Online

ACCESS |

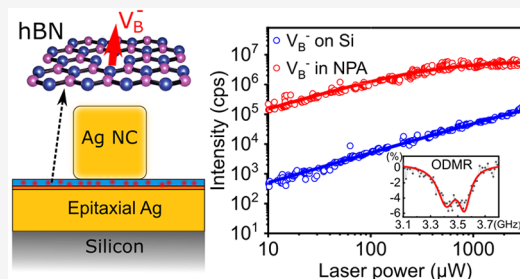
Metrics & More

Article Recommendations

Supporting Information

**ABSTRACT:** The negatively charged boron vacancy ( $V_B^-$ ) defect in hexagonal boron nitride (hBN) with optically addressable spin states has emerged due to its potential use in quantum sensing. Remarkably,  $V_B^-$  preserves its spin coherence when it is implanted at nanometer-scale distances from the hBN surface, potentially enabling ultrathin quantum sensors. However, its low quantum efficiency hinders its practical applications. Studies have reported improving the overall quantum efficiency of  $V_B^-$  defects with plasmonics; however, the overall enhancements of up to 17 times reported to date are relatively modest. Here, we demonstrate much higher emission enhancements of  $V_B^-$  with low-loss nanopatch antennas (NPAs). An overall intensity enhancement of up to 250 times is observed, corresponding to an actual emission enhancement of  $\sim 1685$  times by the NPA, along with preserved optically detected magnetic resonance contrast. Our results establish NPA-coupled  $V_B^-$  defects as high-resolution magnetic field sensors and provide a promising approach to obtaining single  $V_B^-$  defects.

**KEYWORDS:** two-dimensional materials, hBN, plasmonics, nanocavities, spin defects, quantum sensing



Solid-state quantum emitters (QEs) are the central building blocks for emerging quantum technologies, including quantum information processing, quantum communication, and quantum sensing.<sup>1–4</sup> In recent years, significant effort has been made with the development of QEs in two-dimensional van der Waals (vdW) materials such as transition-metal dichalcogenides (TMDC)<sup>5,6</sup> and hexagonal boron nitride (hBN).<sup>7,8</sup> The two-dimensional nature of these host materials and their robust chemical properties offer unparalleled advantages for integrating these QEs with plasmonic and photonic structures<sup>9</sup> into hybrid quantum devices. Specifically, hBN has emerged as a promising platform that hosts QEs with remarkable properties such as strain-<sup>10</sup> and electric-field-tunable<sup>11</sup> optical constants, emission ranging from ultraviolet<sup>12</sup> to near-infrared<sup>13</sup> wavelengths, and spin-selective optical transitions.<sup>14</sup> Consequently, a significant amount of research has been focused on understanding the properties of these defects,<sup>15–19</sup> deterministic creation processes,<sup>20–24</sup> and their integration with photonic structures.<sup>25–28</sup>

Recently, the negatively charged boron-vacancy ( $V_B^-$ ) spin defect (Figure 1a) in hBN<sup>15–19,29–31</sup> has been widely studied for its potential as a quantum sensor for magnetic fields, temperature, pressure, and nuclear spins.<sup>32–35</sup> The  $V_B^-$  defect has a ground-state splitting energy  $D_{GS}/h \approx 3.5$  GHz<sup>29,36</sup> and a spin coherence time  $T_2 \approx 1\ \mu s$  at ambient conditions<sup>29,37</sup> up to

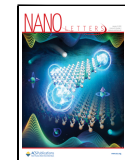
a shallow implantation depth of  $\sim 3$  nm.<sup>37</sup> The ground-state spin population can be initialized and read out optically by virtue of its spin-dependent nonradiative channels (Figure 1b). This development, combined with the facile integration of few-layer hBN with other vdW materials, can enable quantum sensing at approximately nanometer scale distances.

Despite the great potential of  $V_B^-$  defects, their sensitivity to external fields is limited by poor optical quantum efficiency<sup>15</sup> and a weak photoluminescence (PL) signal. Improving the overall quantum efficiency by accelerating the photon emission rate, while retaining the spin properties, constitutes a major task in developing practical quantum sensors with  $V_B^-$  defects. The photon emission rate can be enhanced by coupling to plasmonic structures. The intense local electromagnetic field and subwavelength mode confinement enabled by plasmonics increase both the excitation and spontaneous emission rate of an emitter, hence producing enhanced fluorescence rates.<sup>38–40</sup>

Received: August 4, 2022

Revised: November 9, 2022

Published: November 16, 2022



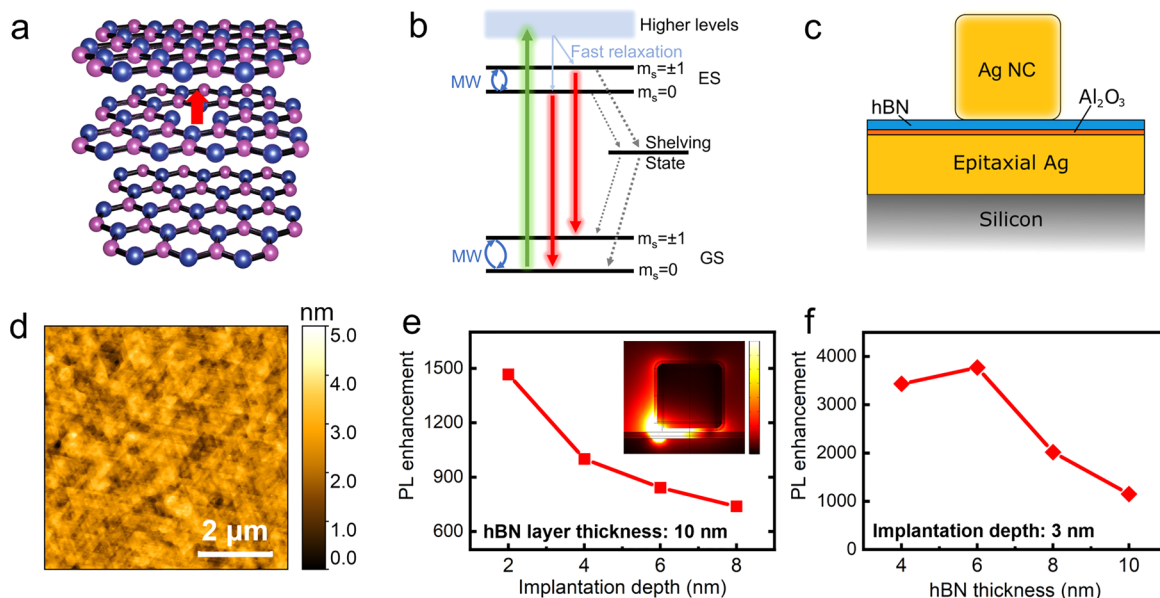


**Figure 1.** (a) Illustration of the atomic structure of  $V_B^-$  in hBN. Boron atoms are shown in purple, while nitrogen atoms are shown in blue. (b) Schematic of the electronic spin levels of  $V_B^-$ . (c) NPA structure adopted in this study, composed of an epitaxial silver film grown on silicon, a 3 nm thick  $\text{Al}_2\text{O}_3$  spacer layer, an hBN layer doped with  $V_B^-$  defects and a single-crystal silver nanocube on top. (d) AFM scan taken from the epitaxial silver film (65 nm in thickness), revealing a surface roughness of 0.32 nm. (e, f) Simulated PL enhancement factors of an NPA-coupled  $V_B^-$  defect at 800 nm as a function of the  $V_B^-$  implantation depth (e) and the hBN layer thickness (f). In (e), the hBN layer thickness is fixed at 10 nm. Inset: normalized electric field distribution in a NPA obtained from FEM models. Color scale range:  $(0-8) \times 10^{32} \text{ V/m}$ . In (f), the implantation depth of  $V_B^-$  is kept at 3 nm.

Previous demonstrations have explored this idea by coupling  $V_B^-$  defects with nanopatch antennas (NPAs)<sup>41</sup> and gold films,<sup>37</sup> with an overall intensity enhancement of up to 17 times. This estimate corresponds to an actual enhancement factor of ~100 in the NPA configuration, considering the ratio of laser spot size and NPA area.

The magnitude of plasmonic enhancement strongly depends on the type and quality of plasmonic materials utilized. Employing plasmonic materials with low optical losses can greatly improve the efficiency of plasmonic cavities,<sup>42</sup> leading to higher Purcell enhancements. This study demonstrates this effect by coupling  $V_B^-$  defects with a resonant nanoplasmionic cavity in the NPA configuration. Unlike previous works where gold films were employed, we use an epitaxially grown silver film<sup>43,44</sup> with superior optical properties.<sup>45,46</sup> By carefully designing and assembling the NPA, we achieve an actual emission enhancement of  $V_B^-$  defects of ~1685 times, which is more than 1 order of magnitude improvement over previous results (~100).<sup>37,41,47</sup> The demonstrated Purcell enhancement and preserved ODMR contrast significantly improve the sensitivity of  $V_B^-$  for advanced sensing applications. Furthermore, it holds great promise for isolating single  $V_B^-$  defects, which has not yet been realized and will further extend the application of  $V_B^-$  in the field of quantum information.

We focus on hBN flakes with thicknesses of <10 nm containing  $V_B^-$  defects induced by helium ion implantation.<sup>37</sup> To assemble NPAs, thin hBN flakes are sandwiched between a single-crystal silver nanocube and a silver film coated with a thin alumina spacer layer (Figure 1c). Silver is well-known to be the best plasmonic material at visible and near-infrared frequencies due to the lowest loss at these frequencies among metals.<sup>48,49</sup> We use epitaxially grown silver films of high crystalline quality, enabling low intrinsic loss and superior plasmonic enhancement.<sup>45,50</sup> Their superior quality is con-

firmed by ellipsometry measurements (Section 3 in the Supporting Information) and atomic force microscopy (AFM) measurements, where a film roughness of ~0.3 nm (Figure 1d) is observed. While the exact orientation of the  $V_B^-$  optical transition dipole<sup>41,51</sup> is not *a priori* known, the gap plasmon mode in the NPA configuration is expected to predominantly enhance its vertically oriented component.

To achieve the best plasmonic enhancement of  $V_B^-$  emission, we consider optimizing two parameters in the NPA design using the finite-element method (FEM) in COMSOL Multiphysics (Section 4 in the Supporting Information): (i) the implantation depth of  $V_B^-$  defects, which determines the vertical location of  $V_B^-$  in the gap, and (ii) the hBN layer thickness, which determines the gap size. The optimization cycle calculates the fluorescence enhancement of  $V_B^-$  emission as a function of both parameters, using the enhancement as a figure of merit. As shown in Figure 1e, the fluorescence enhancement decreases monotonically with increasing implantation depth for a fixed hBN layer thickness. Intuitively, this can be understood by considering that deeper implantation brings  $V_B^-$  defects closer to the silver film, resulting in quenched  $V_B^-$  emission coupled with surface plasmon polaritons (SPPs).<sup>52</sup> In contrast, shallow implantation positions the  $V_B^-$  defects closer to the silver nanocube, which efficiently outcoupling the radiation into far-field modes. In our experiments,  $V_B^-$  defects are implanted at ~3 nm<sup>37</sup> depth from the surface with helium ions at 300 eV. Figure 1f shows the fluorescence enhancement peaks at 6 nm flake thickness. Further reducing the hBN thickness results in decreased fluorescence, likely due to a significant rise in Ohmic losses in the metal film.<sup>53</sup> Therefore, hBN flakes that are ~6 nm thick with  $V_B^-$  defects implanted at 3 nm from the surface are the most desirable in this study.

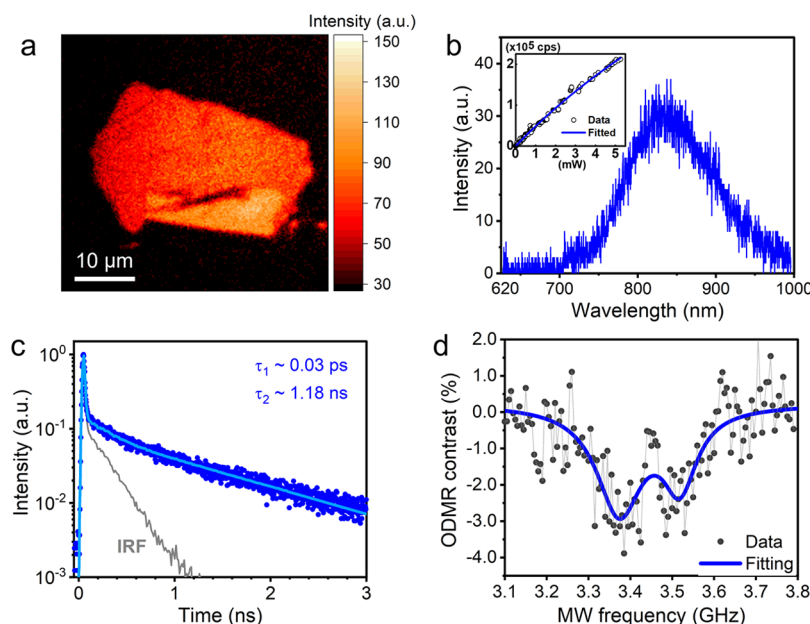


**Figure 2.** Photophysical properties of  $V_B^-$  defects in hBN on  $\text{SiO}_2/\text{Si}$ . (a) Photoluminescence (PL) map collected from an hBN flake containing ensembles of  $V_B^-$  defects. The map was obtained under 532 nm CW laser excitation at 1 mW power at the objective. AFM characterization and thickness measurements of the flake can be found in Figure S5 (Supporting Information), showing a layer thickness of 6.5 nm. (b) Background-subtracted emission spectrum of  $V_B^-$  defects from the hBN flake shown in (a) Inset: background-subtracted fluorescence saturation curve of  $V_B^-$  defects with a saturation count of 1.14 Mcps at 22.6 mW. (c) Time-resolved fluorescence decay of  $V_B^-$  defects (dark blue dots) under the excitation of a 520 nm fs pulsed laser. The data are fitted with a biexponential decay function (solid light blue line) convoluted with the instrumental response function (IRF) (solid gray line). Fitted time constants are shown in the graph. (d) CW ODMR spectrum of  $V_B^-$  (black dots) at 1 mW laser excitation power. The solid blue line is a double-Lorentzian fitting curve, revealing an ODMR contrast of 3%.

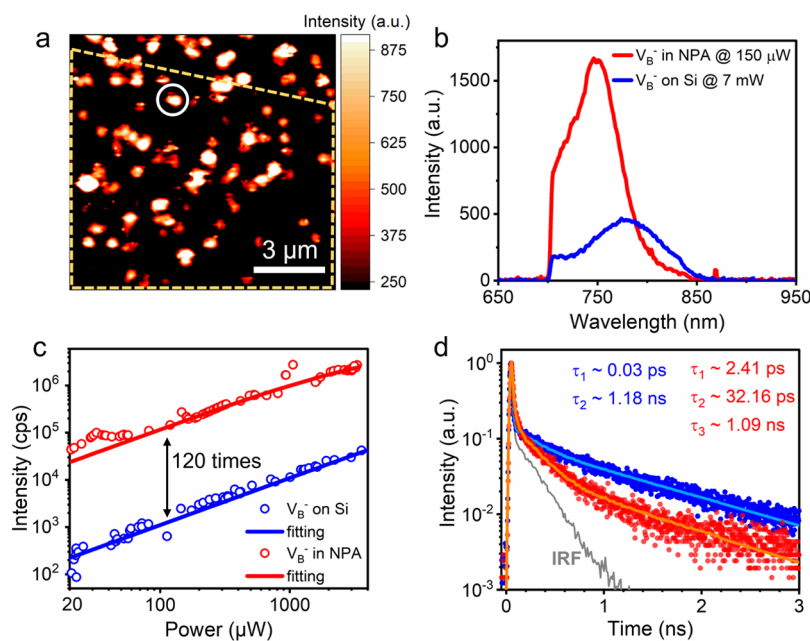


**Figure 3.** Photophysical properties of NPA-coupled  $V_B^-$  emitters. (a) PL map taken from part of an hBN flake (enclosed with an orange dashed line) that was implanted with  $V_B^-$  defects and sandwiched between randomly formed NPAs. Figure S6 (Supporting Information) is rescaled to better show the hBN flake under investigation. (b) Background-subtracted emission spectra of NPA-coupled  $V_B^-$  emitters (solid red line, measured from area circled in white in (a)) and uncoupled  $V_B^-$  emitters from the same flake on a  $\text{SiO}_2/\text{Si}$  substrate prior to the transfer (solid blue line). The corresponding excitation laser powers are indicated in the graph. Note that the emission peak of uncoupled  $V_B^-$  defects here is slightly shifted compared to the spectrum shown in Figure 2b. This is mostly caused by varied implantation doses (Section 7 in the Supporting Information). (c) Background-subtracted saturation plots of NPA-coupled (circled in white in (a)) and uncoupled  $V_B^-$  emitters, shown as red and blue circles, respectively. The solid red and blue lines depict their numerically fitted trends. (d) Fluorescence decay of NPA-coupled  $V_B^-$  emitters (red dots) under pulsed laser excitation. The decay is approximated by a triexponential decay function (solid orange line) convoluted with the instrumental response function (IRF) (solid gray line) with time constants shown in red in the graph. The blue dots and curve (along the two decay time constants, depicted in blue) are taken from Figure 2c for comparison.

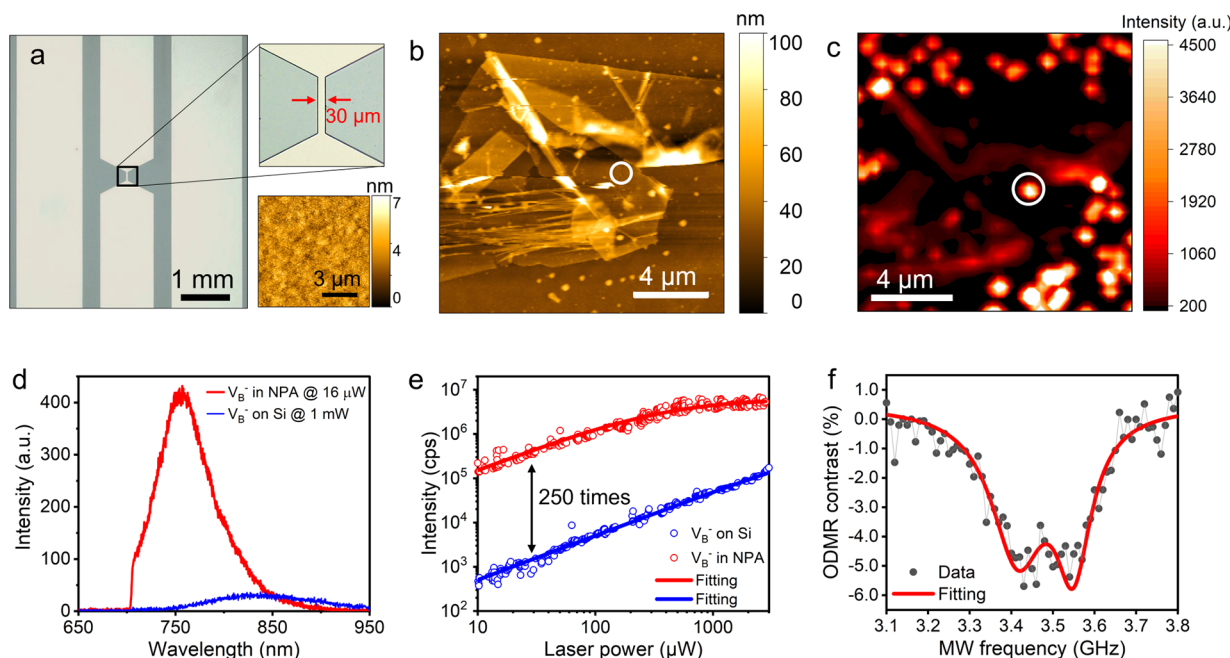


**Figure 4.** (a) (left) Optical image of the microwave waveguide fabricated on a 300 nm thick silver film grown epitaxially on silicon. The bright and dark regions represent silver and silicon, respectively. (top right) Enlarged optical view of the central neck region of the waveguide, showing a neck width of 30  $\mu\text{m}$ . (bottom right) AFM scan from the neck region of the waveguide. A surface roughness of 0.91 nm is obtained. (b) AFM scan of an hBN flake after it is transferred onto the neck region of the microwave waveguide. This is the same flake shown in Figure 2a. (c) PL map of the area containing the hBN flake after drop-casting silver nanocubes, collected along the same orientation as in (b). Due to stronger fluorescence from folds/wrinkles on hBN, the flake location can be identified by matching the fluorescence pattern with the AFM map in (b). The NPA circled in white is also circled in (b) to help understand the matching of two maps. (d) Background-subtracted emission spectra of NPA-coupled V<sub>B</sub><sup>-</sup> emitters (solid red line, circled in white in (c)) and uncoupled V<sub>B</sub><sup>-</sup> emitters from the same flake on a SiO<sub>2</sub>/Si substrate prior to the transfer (solid blue line). The corresponding excitation laser powers are indicated in the graph. (e) Background-subtracted saturation curves of NPA-coupled and uncoupled V<sub>B</sub><sup>-</sup> emitters, shown as red and blue circles, respectively. The solid red and blue lines are fittings. An emission enhancement of  $\sim$ 250 times is observed at laser powers  $<300 \mu\text{W}$ . (f) CW ODMR spectrum of V<sub>B</sub><sup>-</sup> (black dots) at a 40 mW microwave driving power and 30  $\mu\text{W}$  laser excitation power. The solid red line is a double-Lorentzian fitting curve that yields an ODMR contrast of 6%.

We begin with hBN flakes that are mechanically exfoliated from high-quality hBN crystals onto SiO<sub>2</sub> (300 nm thick)-coated Si substrates. Flat hBN flakes with suitable thicknesses ( $\sim$ 6 nm) are identified and implanted to induce V<sub>B</sub><sup>-</sup> defects. A photoluminescence (PL) map collected from a 6 nm thick flake in Figure 2a after ion implantation confirms the formation of a uniform layer of fluorescing V<sub>B</sub><sup>-</sup> emitters. Under 532 nm laser excitation, V<sub>B</sub><sup>-</sup> defects show a broad emission spectrum in the range of 700–1000 nm and a saturation intensity of 1.14 Mcts/s (Figure 2b), consistent with previous reports.<sup>36,37</sup> The fluorescence lifetime of V<sub>B</sub><sup>-</sup> can be extracted from the time-resolved fluorescence decay upon pulsed laser excitation, as illustrated in Figure 2c. The fluorescence decay is fitted using a biexponential function with  $\tau_1 = 0.03 \text{ ps}$  and  $\tau_2 = 1.18 \text{ ns}$ . The slower component,  $\tau_2$ , is assigned to be the lifetime of V<sub>B</sub><sup>-</sup> and agrees well with reported values.<sup>41</sup> The faster component,  $\tau_1$ , is not yet well understood but could originate from the instrument itself or organic residues on the substrate from the hBN transfer process. Finally, ODMR measurements are performed by delivering microwaves through a copper wire positioned close to the hBN flake, and an ODMR contrast of  $\sim$ 3% is observed (Figure 2d).

We transfer the precharacterized thin hBN flakes containing V<sub>B</sub><sup>-</sup> defects onto an alumina-coated epitaxial silver film (65 nm in thickness). Finally, silver nanocubes with an edge length of  $\sim$ 100 nm are drop-casted to form NPAs on hBN. Due to the high-density, uniform distribution of V<sub>B</sub><sup>-</sup> defects in hBN flakes, manipulation or deterministic placing of nanocubes is not

required in this study. Nevertheless, the more controlled coupling of silver nanocubes with V<sub>B</sub><sup>-</sup> defects at specific locations could be realized using two possible techniques. One is to create V<sub>B</sub><sup>-</sup> defects at designated positions with a focused helium ion beam with high spatial precision; another is to pattern hBN flakes that are uniformly doped with V<sub>B</sub><sup>-</sup> defects into nanoscale structures, such as nanodisk arrays. Both approaches can enable the deterministic, and potentially optimized, coupling of V<sub>B</sub><sup>-</sup> defects with nanocubes in combination with techniques (e.g., AFM<sup>54,55</sup>) to manipulate nanocubes.

Figure 3a shows a PL map from an area where an hBN flake (6.5 nm in thickness; see the Supporting Information) has randomly distributed NPAs. V<sub>B</sub><sup>-</sup> defects in NPAs (referred to as NPA-coupled defects) are then characterized and compared with V<sub>B</sub><sup>-</sup> emitters on SiO<sub>2</sub>/Si substrates (referred to as uncoupled defects). Due to the plasmonic enhancement of NPA, a significantly lower laser power is needed for optical characterization. Figure 3b shows the emission spectrum from NPA-coupled defects (circled in red in Figure 3a) along with a spectrum collected from the same hBN flake on a SiO<sub>2</sub>/Si substrate. The emission intensity from NPA-coupled V<sub>B</sub><sup>-</sup> defects is significantly higher than that of uncoupled defects, despite the nearly 50-fold smaller excitation laser power. The peak emission wavelength of NPA-coupled V<sub>B</sub><sup>-</sup> defects is slightly blue shifted due to coupling with the cavity mode, as discussed in detail in Section 6 in the Supporting Information. To better quantify the enhancement factor, saturation curves of

NPA-coupled and uncoupled  $V_B^-$  emitters are compared in Figure 3c within a broad range of laser powers, where an overall intensity enhancement of  $\sim 120$  times is observed—a significantly higher plasmonic enhancement for  $V_B^-$  defects than those in previous reports.<sup>37,41</sup>

The improved brightness of plasmon-enhanced QEs is typically accompanied by lifetime shortening. We collected the fluorescence decay curve of  $V_B^-$  emitters coupled to the above NPA and compared it to that from uncoupled  $V_B^-$  emitters on  $\text{SiO}_2/\text{Si}$ . As shown in Figure 3d, the decay curve cannot be straightforwardly fitted with a biexponential decay as in the case of uncoupled  $V_B^-$  defects. This difficulty comes from the nonuniform PL enhancements experienced by  $V_B^-$  emitters within the excitation laser spot (spot size  $> \pi \times 260 \text{ nm}^2 \approx 2.1 \times 10^5 \text{ nm}^2$  at a wavelength of 520 nm), which is at least 1 order of magnitude larger than the silver nanocube cross-section ( $10^4 \text{ nm}^2$ ). This observation is supported by the fact that the decay curve is well fitted using a triexponential function with  $\tau_1 = 2.41 \text{ ps}$ ,  $\tau_2 = 33.16 \text{ ps}$ , and  $\tau_3 = 1.09 \text{ ns}$ . While the fastest component  $\tau_1$  is unrelated to the  $V_B^-$  decay dynamics,  $\tau_2$  and  $\tau_3$  can be attributed to lifetimes of strongly enhanced (NPA-coupled, under the nanocube) and weakly enhanced (outside the nanocube)  $V_B^-$  emitters, respectively. Therefore, the lifetime shortening of NPA-enhanced  $V_B^-$  is 36 times. As expected, this is smaller than the PL enhancement factor due to the high intrinsic nonradiative decay rates of  $V_B^-$ .<sup>15,38</sup> The weakly enhanced  $V_B^-$  emitters on Ag film only without NPAs (Section 9 in the Supporting Information) show a slight lifetime shortening (1.1 times). As discussed later, this enhancement comes from the silver film's localized surface plasmon modes (LSPs).

For practical quantum sensing, it is critical to ensure that the spin contrast and PL intensity are significant. Due to the high reflectivity of the silver substrate and silver nanocubes, microwave delivery by a copper wire on the sample surface is a nonviable solution. We circumvent this issue by using lithographically patterned waveguide-mediated microwave delivery.<sup>33,34,37</sup> A coplanar waveguide structure offers more efficient control of the defect spins with the “in-plane” orientation of the microwave fields driving the “out-of-plane” spins.

Figure 4a shows an optical image of the silver waveguide (see the design in Figure S7 in the Supporting Information). Notably, the quality of epitaxial silver films that is critical to ensure high plasmonic enhancement is mostly preserved after all fabrication steps, as confirmed by AFM (Figure 4a, bottom). To achieve the best ODMR results, we transfer an implanted hBN flake (6.5 nm in thickness; see the Supporting Information) onto the central neck region of the waveguide. Although the transfer process introduces wrinkles to the flake, there are flat regions suitable for NPA fabrication (Figure 4b). Figure 4c is a PL map of the flake showing well-isolated NPAs after drop-casting silver nanocubes. Specifically, the NPA circled in red is studied systematically, with its spectrum and saturation curve plotted in red in Figure 4d,e, respectively, along with the data collected from the same flake on a  $\text{SiO}_2/\text{Si}$  substrate. Again, we observe a significant overall emission intensity enhancement from NPA-coupled  $V_B^-$  emitters, around 250 times at low laser powers ( $< 300 \mu\text{W}$ ). The enhancement factor slightly decreases at higher laser powers as NPA-coupled  $V_B^-$  emitters saturate earlier than uncoupled emitters. The fluorescence decay behavior of the NPA-coupled emitters is also measured and is presented in the Supporting

Information. Finally, ODMR measurements are performed by exciting the hBN sample with microwaves through the silver waveguide, yielding an ODMR contrast of  $\sim 6\%$  (Figure 4f).

While the intensity enhancement obtained with the waveguide structure is higher than that from the NPA on a planar silver film discussed earlier, the underlying physics is fundamentally the same. The difference in enhancement factor can be attributed to the local variation in the optical properties of NPAs, such as the roughness of silver, roughness of hBN, quality of silver nanocubes, spatial distribution of  $V_B^-$  emitters under nanocubes, etc. This difference is also reflected in the variation of enhancement factors that we observed experimentally from several NPAs located on the same hBN flake (Section 8 in the Supporting Information). Nevertheless, the significant plasmonic enhancement combined with the ODMR contrast from the NPA-coupled defects in the waveguide presents a significant advancement for sensing applications.

In addition to optical characterization of NPA-coupled  $V_B^-$  emitters, we also examined  $V_B^-$  emitters that are only coupled with the silver film to isolate their contributions to the plasmonic enhancement. As demonstrated in Section 9 in the Supporting Information, the emission intensity of silver-film-coupled  $V_B^-$  emitters is slightly higher than that of uncoupled  $V_B^-$  defects on  $\text{SiO}_2/\text{Si}$ , and an  $\sim 6$ -fold intensity enhancement by the silver film is extracted from the saturation curves. Such enhancement is likely related to the excitation of localized surface plasmon (LSP) modes on the silver film. Ideally, plasmonic enhancement is not expected from smooth, crystalline metal films, which only support propagating surface plasmon modes that weakly couple to photons due to momentum mismatch. In practice, however, even high-quality metal films show roughness at the nanoscale, potentially relaxing the momentum mismatch condition.<sup>37</sup> The results above indicate that the gap plasmon modes in the NPA play a dominant role in enhancing  $V_B^-$  emission in this work, rather than the LSP modes in the silver film.

To quantify the actual enhancement factor, we consider  $V_B^-$  defects under the silver nanocube that are enhanced by the gap plasmon modes of the NPA and the rest of the defects within the pump laser spot that are enhanced only by the silver film. Hence, the actual enhancement factor by NPA can be estimated based on the expression

$$\frac{A_{\text{cube}}P_{\text{NPA}} + (A_{\text{laser}} - A_{\text{cube}})P_{\text{Ag}}}{A_{\text{laser}}} = P_{\text{ave}}$$

where  $P_{\text{Ag}} = 6$  and  $P_{\text{ave}} = 250$  refer to the enhancement factor by the silver film and the overall enhancement factor measured experimentally from the laser spot area containing an NPA, respectively, and  $A_{\text{cube}}$  and  $A_{\text{laser}}$  are the silver nanocube facet area ( $A_{\text{cube}} = 10^4 \text{ nm}^2$ ) and the diffraction-limited laser spot area for a 532 nm pump laser ( $\text{NA} = 0.9$ ,  $A_{\text{laser}} = 6.88 \times 10^4 \text{ nm}^2$ ). Combining the values above, the actual enhancement factor by NPA is calculated to be  $P_{\text{NPA}} = 1685$ . While the calculation above does not include factors such as the exact optical dipole orientation of  $V_B^-$ , the spatial heterogeneity of  $V_B^-$  emitters, the effect of laser beam shape, etc., it clearly demonstrates an NPA-assisted intensity enhancement of  $V_B^-$  emission by more than 3 orders of magnitude. The achieved enhancement significantly improves the overall quantum efficiency of  $V_B^-$  by boosting its radiative decay rate, hence

providing a promising way to obtain single  $V_B^-$  emitters with observable brightness.

We observe slightly higher ODMR contrasts from NPA-coupled emitters (6%) and silver-film-coupled emitters (11%, Figure S15d in the Supporting Information) as compared to  $V_B^-$  emitters on  $\text{SiO}_2/\text{Si}$  (~3%) due to higher microwave field strengths in the waveguide configuration.

The most important figure of merit in practical sensing applications is the sensitivity to external stimuli. In quantum sensing of external magnetic fields, the sensitivity is defined as the smallest magnetic field that can be measured in 1 s.<sup>4</sup> In the ODMR-based sensing scheme,<sup>4</sup> the sensitivity ( $S$ ) is closely related to the number of photons detected ( $N$ ), the ODMR contrast ( $C$ ), and the line width of the ODMR signal ( $\Delta\nu$ ) as  $S \approx \frac{\Delta\nu}{\sqrt{NC}}$ . A higher microwave/laser power can lead to a higher contrast/PL strength at the cost of deteriorating the ODMR line width and sample heating. In our experiment, we demonstrate a PL enhancement of ~1685 times without significant deteriorations of the ODMR line width ( $\Delta\nu \approx 100$  MHz) and spin contrast ( $C \approx 6\%$ ) for NPA-coupled  $V_B^-$  defects. This leads to an improvement in  $S$  of about  $\sqrt{1685} \approx 41$  times compared to uncoupled  $V_B^-$  defects. For the CW-ODMR scheme, the absolute value of  $S$  is calculated to be  $\sim 138 \frac{\mu T}{\sqrt{Hz}}$  for NPA-coupled  $V_B^-$  at a laser power of 30  $\mu\text{W}$  and microwave power of 40 mW with known parameters.<sup>4,56</sup> This value of  $S$  is comparable to the sensitivity of  $V_B^-$  reported by Gottscholl *et al.*<sup>32</sup> Gao *et al.*<sup>37</sup> have reported higher sensitivities of  $V_B^-$  after optimizing the laser and microwave powers. However, note that those values of  $S$  were achieved at a much higher laser power (>1 mW) and microwave power (0.25 W), as well as for a larger hBN flake thickness (35 nm).

Compared to the reports above, our configuration processes the following unique advantages: (1) a much smaller laser power required for achieving effective sensing, which avoids the detrimental effects of high driving powers; (2) a much higher spatial resolution as defined by the silver nanocube dimension (~100 nm) and an extremely small separation distance between the probing spin and material of interest (3 nm). In the case of sensing magnetic excitations,<sup>57</sup> this sample–probe distance not only improves the strength of stray magnetic fields but also determines the wavelength of the excitations that couple with the spin transition. Furthermore, measuring stray magnetic fields emanating from magnetic materials at a close distance of ~3 nm enables advanced probes for previously unexplored phenomena. In a future study, the sensitivity of NPA-coupled  $V_B^-$  emitters can be further improved by optimizing the laser/microwave powers and the implantation doses.

In conclusion, we have demonstrated fluorescence enhancement of ensembles of  $V_B^-$  defects in a thin hBN flake by coupling them to silver-based nanopatch antennas (NPAs) with an overall PL intensity enhancement of up to 250 times, corresponding to a 1685-fold actual PL enhancement by the NPA. We take advantage of epitaxial silver films in our NPA fabrication, enabling ultralow optical losses and hence higher Purcell factors. Furthermore,  $V_B^-$  defects retain an ODMR contrast of 6% after being coupled to NPAs. The preserved ODMR contrast and the significant PL enhancement make NPA-coupled  $V_B^-$  defects effective quantum sensors. This is confirmed by our sensitivity evaluation of NPA-coupled  $V_B^-$

emitters, where a magnetic field sensitivity of  $138 \frac{\mu T}{\sqrt{Hz}}$  is calculated at a laser power of 30  $\mu\text{W}$ . The small thickness of hBN flakes (<10 nm) involved in the NPA configuration also offers unique advantages to probing weak fields very close to the sample of interest. Aside from advanced sensing applications, the significant PL enhancement achieved in our NPA structure provides a promising way to access single  $V_B^-$  spin defects, an important step to exploit the potential of  $V_B^-$  in quantum information science and technologies.

## ASSOCIATED CONTENT

### Supporting Information

The Supporting Information is available free of charge at <https://pubs.acs.org/doi/10.1021/acs.nanolett.2c03100>.

Details of material preparation, sample fabrication, and experimental setup, optical properties of epitaxial silver films, details of the FEM simulations, and additional information on hBN flakes and NPAs studied in this work ([PDF](#))

## AUTHOR INFORMATION

### Corresponding Author

Vladimir M. Shalaev – Birck Nanotechnology Center, Elmore Family School of Electrical and Computer Engineering, and Purdue Quantum Science and Engineering Institute (PQSEI), Purdue University, West Lafayette, Indiana 47907, United States; The Quantum Science Center (QSC), a National Quantum Information Science Research Center of the U.S. Department of Energy (DOE), Oak Ridge National Laboratory, Oak Ridge, Tennessee 37831, United States; Email: [shalaev@purdue.edu](mailto:shalaev@purdue.edu)

### Authors

Xiaohui Xu – School of Materials Engineering, Purdue University, West Lafayette, Indiana 47907, United States; Birck Nanotechnology Center, Purdue University, West Lafayette, Indiana 47907, United States; [orcid.org/0000-0003-0369-3917](https://orcid.org/0000-0003-0369-3917)

Abhishek B. Solanki – Birck Nanotechnology Center and Elmore Family School of Electrical and Computer Engineering, Purdue University, West Lafayette, Indiana 47907, United States

Demid Sychev – Birck Nanotechnology Center and Elmore Family School of Electrical and Computer Engineering, Purdue University, West Lafayette, Indiana 47907, United States

Xingyu Gao – Department of Physics and Astronomy, Purdue University, West Lafayette, Indiana 47907, United States

Samuel Peana – Birck Nanotechnology Center and Elmore Family School of Electrical and Computer Engineering, Purdue University, West Lafayette, Indiana 47907, United States

Aleksandr S. Baburin – FMN Laboratory, Bauman Moscow State Technical University, Moscow 105005, Russia; Dukhov Automatics Research Institute (VNIIA), Moscow 127055, Russia

Karthik Pagadala – Birck Nanotechnology Center and Elmore Family School of Electrical and Computer Engineering, Purdue University, West Lafayette, Indiana 47907, United States; [orcid.org/0000-0003-2152-640X](https://orcid.org/0000-0003-2152-640X)

Zachariah O. Martin – Birck Nanotechnology Center and Elmore Family School of Electrical and Computer

Engineering, Purdue University, West Lafayette, Indiana 47907, United States

Sarah N. Chowdhury – Birck Nanotechnology Center and Elmore Family School of Electrical and Computer Engineering, Purdue University, West Lafayette, Indiana 47907, United States;  [orcid.org/0000-0002-1336-4511](https://orcid.org/0000-0002-1336-4511)

Yong P. Chen – Birck Nanotechnology Center, Elmore Family School of Electrical and Computer Engineering, Department of Physics and Astronomy, and Purdue Quantum Science and Engineering Institute (PQSEI), Purdue University, West Lafayette, Indiana 47907, United States; The Quantum Science Center (QSC), a National Quantum Information Science Research Center of the U.S. Department of Energy (DOE), Oak Ridge National Laboratory, Oak Ridge, Tennessee 37831, United States; Institute of Physics and Astronomy and Villum Center for Hybrid Quantum Materials and Devices, Aarhus University, 8000 Aarhus-C, Denmark; WPI-AIMR International Research Center for Materials Sciences, Tohoku University, Sendai 980-8577, Japan

Takashi Taniguchi – International Center for Materials Nanoarchitectonics, National Institute for Materials Science, Tsukuba 305-0044, Japan;  [orcid.org/0000-0002-1467-3105](https://orcid.org/0000-0002-1467-3105)

Kenji Watanabe – Research Center for Functional Materials, National Institute for Materials Science, Tsukuba 305-0044, Japan;  [orcid.org/0000-0003-3701-8119](https://orcid.org/0000-0003-3701-8119)

Ilya A. Rodionov – FMN Laboratory, Bauman Moscow State Technical University, Moscow 105005, Russia; Dukhov Automatics Research Institute (VNIIA), Moscow 127055, Russia;  [orcid.org/0000-0002-8931-5142](https://orcid.org/0000-0002-8931-5142)

Alexander V. Kildishev – Birck Nanotechnology Center, Elmore Family School of Electrical and Computer Engineering, and Purdue Quantum Science and Engineering Institute (PQSEI), Purdue University, West Lafayette, Indiana 47907, United States;  [orcid.org/0000-0002-8382-8422](https://orcid.org/0000-0002-8382-8422)

Tongcang Li – Birck Nanotechnology Center, Elmore Family School of Electrical and Computer Engineering, Department of Physics and Astronomy, and Purdue Quantum Science and Engineering Institute (PQSEI), Purdue University, West Lafayette, Indiana 47907, United States;  [orcid.org/0003-3308-8718](https://orcid.org/0003-3308-8718)

Pramey Upadhyaya – Elmore Family School of Electrical and Computer Engineering and Purdue Quantum Science and Engineering Institute (PQSEI), Purdue University, West Lafayette, Indiana 47907, United States; The Quantum Science Center (QSC), a National Quantum Information Science Research Center of the U.S. Department of Energy (DOE), Oak Ridge National Laboratory, Oak Ridge, Tennessee 37831, United States

Alexandra Boltasseva – School of Materials Engineering, Purdue University, West Lafayette, Indiana 47907, United States; Birck Nanotechnology Center, Elmore Family School of Electrical and Computer Engineering, and Purdue Quantum Science and Engineering Institute (PQSEI), Purdue University, West Lafayette, Indiana 47907, United States; The Quantum Science Center (QSC), a National Quantum Information Science Research Center of the U.S. Department of Energy (DOE), Oak Ridge National Laboratory, Oak Ridge, Tennessee 37831, United States;  [orcid.org/0001-8905-2605](https://orcid.org/0001-8905-2605)

Complete contact information is available at:  
<https://pubs.acs.org/10.1021/acs.nanolett.2c03100>

## Author Contributions

X.X., A.B.S., and D.S. initiated and designed the experiments. X.G. performed the SRIM simulations and ion implantation. T.T. and K.W. contributed to the growth of high-quality hBN crystals. A.B.S., X.X., and D.S. exfoliated, characterized, and transferred hBN flakes. X.X. performed the numerical simulations and AFM measurements. A.S.B. grew and characterized the epitaxial silver films. X.X., A.B.S., D.S., and X.G. performed optical characterizations of boron vacancy defects. S.P., X.X., and K.P. fabricated the silver microwave waveguides. K.P. performed the ellipsometry measurements. Z.O.M. and S.N.C. deposited the alumina spacer layer. X.X. and A.B.S. wrote the initial draft of the paper. V.M.S. and A.B. supervised the project. All authors contributed to the discussion and writing of the paper.

## Author Contributions

X.X. and A.B.S. contributed equally.

## Notes

The authors declare no competing financial interest.

## ACKNOWLEDGMENTS

The authors acknowledge Vahagn Mkhitaryan and Benjamin Lawrie for helpful discussions on COMSOL simulations and quantum efficiency evaluation of NPA-enhanced  $V_B^-$  emitters. This work was supported by the U.S. Department of Energy (DOE), Office of Science, through the Quantum Science Center (QSC), DE-AC05-00OR22725, National Science Foundation Award 2015025-ECCS, DMR-1747426, and Air Force Office of Scientific Research Award FA9550-22-1-0372. K.W. and T.T. acknowledge support from the JSPS KAKENHI (Grant Nos. 19H05790, 20H00354, and 21H05233). Y.P.C. also thanks the hospitality of NIMS and support of Tohoku AIMR and FriDUO program.

## REFERENCES

- (1) Aharonovich, I.; Englund, D.; Toth, M. Solid-State Single-Photon Emitters. *Nat. Photonics* **2016**, *10* (10), 631–641.
- (2) Weber, J. R.; Koehl, W. F.; Varley, J. B.; Janotti, A.; Buckley, B. B.; Van De Walle, C. G.; Awschalom, D. D. Quantum Computing with Defects. *Proc. Natl. Acad. Sci. U. S. A.* **2010**, *107* (19), 8513–8518.
- (3) Atature, M.; Englund, D.; Vamivakas, N.; Lee, S. Y.; Wrachtrup, J. Material Platforms for Spin-Based Photonic Quantum Technologies. *Nat. Rev. Mater.* **2018**, *3* (5), 38–51.
- (4) Degen, C. L.; Reinhard, F.; Cappellaro, P. Quantum Sensing. *Rev. Mod. Phys.* **2017**, *89* (3), 035002.
- (5) Tonndorf, P.; Schmidt, R.; Schneider, R.; Kern, J.; Buscema, M.; Steele, G. A.; Castellanos-Gomez, A.; van der Zant, H. S. J.; Michaelis de Vasconcellos, S.; Bratschitsch, R. Single-Photon Emission from Localized Excitons in an Atomically Thin Semiconductor. *Optica* **2015**, *2* (4), 347–352.
- (6) Koperski, M.; Nogajewski, K.; Arora, A.; Cherkez, V.; Mallet, P.; Veullien, J. Y.; Marcus, J.; Kossacki, P.; Potemski, M. Single Photon Emitters in Exfoliated WSe<sub>2</sub> Structures. *Nat. Nanotechnol.* **2015**, *10* (6), 503–506.
- (7) Kianinia, M.; Xu, Z. Q.; Toth, M.; Aharonovich, I. Quantum Emitters in 2D Materials: Emitter Engineering, Photophysics, and Integration in Photonic Nanostructures. *Appl. Phys. Rev.* **2022**, *9* (1), 011306.
- (8) Tran, T. T.; Bray, K.; Ford, M. J.; Toth, M.; Aharonovich, I. Quantum Emission from Hexagonal Boron Nitride Monolayers. *Nat. Nanotechnol.* **2016**, *11*, 37–41.

- (9) Peyskens, F.; Chakraborty, C.; Muneeb, M.; Van Thourhout, D.; Englund, D. Integration of Single Photon Emitters in 2D Layered Materials with a Silicon Nitride Photonic Chip. *Nat. Commun.* **2019**, *10*, 4435.
- (10) Mendelson, N.; Doherty, M.; Toth, M.; Aharonovich, I.; Tran, T. T. Strain-Induced Modification of the Optical Characteristics of Quantum Emitters in Hexagonal Boron Nitride. *Adv. Mater.* **2020**, *32* (21), 1908316.
- (11) Mendelson, N.; Xu, Z. Q.; Tran, T. T.; Kianinia, M.; Scott, J.; Bradac, C.; Aharonovich, I.; Toth, M. Engineering and Tuning of Quantum Emitters in Few-Layer Hexagonal Boron Nitride. *ACS Nano* **2019**, *13* (3), 3132–3140.
- (12) Bourrellier, R.; Meuret, S.; Tararan, A.; Stéphan, O.; Kociak, M.; Tizei, L. H. G.; Zobelli, A. Bright UV Single Photon Emission at Point Defects in H-BN. *Nano Lett.* **2016**, *16* (7), 4317–4321.
- (13) Tran, T. T.; Elbadawi, C.; Totonjian, D.; Lobo, C. J.; Grossi, G.; Moon, H.; Englund, D. R.; Ford, M. J.; Aharonovich, I.; Toth, M. Robust Multicolor Single Photon Emission from Point Defects in Hexagonal Boron Nitride. *ACS Nano* **2016**, *10* (8), 7331–7338.
- (14) Liu, W.; Guo, N.-J.; Yu, S.; Meng, Y.; Li, Z.-P.; Yang, Y.-Z.; Wang, Z.-A.; Zeng, X.-D.; Xie, L.-K.; Li, Q.; Wang, J.-F.; Xu, J.-S.; Wang, Y.-T.; Tang, J.-S.; Li, C.-F.; Guo, G.-C. Spin-Active Defects in Hexagonal Boron Nitride. *Mater. Quantum Technol.* **2022**, *2* (3), 032002.
- (15) Reimers, J. R.; Shen, J.; Kianinia, M.; Bradac, C.; Aharonovich, I.; Ford, M. J.; Piecuch, P. Photoluminescence, Photophysics, and Photochemistry of the V<sub>B</sub><sup>-</sup> Defect in Hexagonal Boron Nitride. *Phys. Rev. B* **2020**, *102* (14), 144105.
- (16) Yu, P.; Sun, H.; Wang, M.; Zhang, T.; Ye, X.; Zhou, J.; Liu, H.; Wang, C.-J.; Shi, F.; Wang, Y.; Du, J. Excited-State Spectroscopy of Spin Defects in Hexagonal Boron Nitride. *Nano Lett.* **2022**, *22* (9), 3545–3549.
- (17) Baber, S.; Malein, R. N. E.; Khatri, P.; Keatley, P. S.; Guo, S.; Withers, F.; Ramsay, A. J.; Luxmoore, I. J. Excited State Spectroscopy of Boron Vacancy Defects in Hexagonal Boron Nitride Using Time-Resolved Optically Detected Magnetic Resonance. *Nano Lett.* **2022**, *22* (1), 461–467.
- (18) Mathur, N.; Mukherjee, A.; Gao, X.; Luo, J.; McCullian, B. A.; Li, T.; Vamivakas, A. N.; Fuchs, G. D. Excited-State Spin-Resonance Spectroscopy of V<sub>B</sub><sup>-</sup> Defect Centers in Hexagonal Boron Nitride. *Nat. Commun.* **2022**, *13*, 3233.
- (19) Smart, T. J.; Li, K.; Xu, J.; Ping, Y. Intersystem Crossing and Exciton–Defect Coupling of Spin Defects in Hexagonal Boron Nitride. *npj Comput. Mater.* **2021**, *7*, 59.
- (20) Xu, X.; Martin, Z. O.; Sychev, D.; Lagutchev, A. S.; Chen, Y. P.; Taniguchi, T.; Watanabe, K.; Shalaev, V. M.; Boltasseva, A. Creating Quantum Emitters in Hexagonal Boron Nitride Deterministically on Chip-Compatible Substrates. *Nano Lett.* **2021**, *21* (19), 8182–8189.
- (21) Ziegler, J.; Klais, R.; Blaikie, A.; Miller, D.; Horowitz, V. R.; Alemán, B. J. Deterministic Quantum Emitter Formation in Hexagonal Boron Nitride via Controlled Edge Creation. *Nano Lett.* **2019**, *19* (3), 2121–2127.
- (22) Proscia, N. V.; Shotan, Z.; Jayakumar, H.; Reddy, P.; Cohen, C.; Dollar, M.; Alkauskas, A.; Doherty, M.; Meriles, C. A.; Menon, V. M. Near-Deterministic Activation of Room-Temperature Quantum Emitters in Hexagonal Boron Nitride. *Optica* **2018**, *5* (9), 1128.
- (23) Li, C.; Mendelson, N.; Ritika, R.; Chen, Y.-L.; Xu, Z.-Q.; Toth, M.; Aharonovich, I. Scalable and Deterministic Fabrication of Quantum Emitter Arrays from Hexagonal Boron Nitride. *Nano Lett.* **2021**, *21* (8), 3626–3632.
- (24) Fournier, C.; Plaud, A.; Roux, S.; Pierret, A.; Rosticher, M.; Watanabe, K.; Taniguchi, T.; Buil, S.; Quélin, X.; Barjon, J.; Hermier, J. P.; Delteil, A. Position-Controlled Quantum Emitters with Reproducible Emission Wavelength in Hexagonal Boron Nitride. *Nat. Commun.* **2021**, *12*, 3779.
- (25) Kim, S.; Duong, N. M. H.; Nguyen, M.; Lu, T. J.; Kianinia, M.; Mendelson, N.; Solntsev, A.; Bradac, C.; Englund, D. R.; Aharonovich, I. Integrated on Chip Platform with Quantum Emitters in Layered Materials. *Adv. Opt. Mater.* **2019**, *7* (23), 1901132.
- (26) Froch, J. E.; Kim, S.; Mendelson, N.; Kianinia, M.; Toth, M.; Aharonovich, I. Coupling Hexagonal Boron Nitride Quantum Emitters to Photonic Crystal Cavities. *ACS Nano* **2020**, *14* (6), 7085–7091.
- (27) Elshaari, A. W.; Skalli, A.; Gyger, S.; Nurizzo, M.; Schweickert, L.; Esmaeil Zadeh, I.; Svedendahl, M.; Steinhauer, S.; Zwiller, V. Deterministic Integration of HBN Emitter in Silicon Nitride Photonic Waveguide. *Adv. Quantum Technol.* **2021**, *4* (6), 2100032.
- (28) Li, C.; Fröch, J. E.; Nonahal, M.; Tran, T. N.; Toth, M.; Kim, S.; Aharonovich, I. Integration of HBN Quantum Emitters in Monolithically Fabricated Waveguides. *ACS Photonics* **2021**, *8* (10), 2966–2972.
- (29) Gottscholl, A.; Diez, M.; Soltamov, V.; Kasper, C.; Sperlich, A.; Kianinia, M.; Bradac, C.; Aharonovich, I.; Dyakonov, V. Room Temperature Coherent Control of Spin Defects in Hexagonal Boron Nitride. *Sci. Adv.* **2021**, *7*, abf3630.
- (30) Gao, X.; Pandey, S.; Kianinia, M.; Ahn, J.; Ju, P.; Aharonovich, I.; Shivaram, N.; Li, T. Femtosecond Laser Writing of Spin Defects in Hexagonal Boron Nitride. *ACS Photonics* **2021**, *8* (4), 994–1000.
- (31) Guo, N. J.; Liu, W.; Li, Z. P.; Yang, Y. Z.; Yu, S.; Meng, Y.; Wang, Z. A.; Zeng, X. D.; Yan, F. F.; Li, Q.; Wang, J. F.; Xu, J. S.; Wang, Y. T.; Tang, J. S.; Li, C. F.; Guo, G. C. Generation of Spin Defects by Ion Implantation in Hexagonal Boron Nitride. *ACS Omega* **2022**, *7* (2), 1733–1739.
- (32) Gottscholl, A.; Diez, M.; Soltamov, V.; Kasper, C.; Krauße, D.; Sperlich, A.; Kianinia, M.; Bradac, C.; Aharonovich, I.; Dyakonov, V. Spin Defects in HBN as Promising Temperature, Pressure and Magnetic Field Quantum Sensors. *Nat. Commun.* **2021**, *12* (1), 4480.
- (33) Huang, M.; Zhou, J.; Chen, D.; Lu, H.; McLaughlin, N. J.; Li, S.; Alghamdi, M.; Djugba, D.; Shi, J.; Wang, H.; Du, C. R. Wide Field Imaging of van Der Waals Ferromagnet Fe<sub>3</sub>GeTe<sub>2</sub> by Spin Defects in Hexagonal Boron Nitride. *Nat. Commun.* **2022**, *13* (1), 1–7.
- (34) Healey, A. J.; Scholten, S. C.; Yang, T.; Scott, J. A.; Abrahams, G. J.; Robertson, I. O.; Hou, X. F.; Guo, Y. F.; Rahman, S.; Lu, Y.; Kianinia, M.; Aharonovich, I.; Tetienne, J.-P. Quantum Microscopy with van Der Waals Heterostructures. *arXiv (Mesoscale and Nanoscale Physics)*, December 7, 2021, <http://arxiv.org/abs/2112.03488>.
- (35) Gao, X.; Vaidya, S.; Li, K.; Ju, P.; Jiang, B.; Xu, Z.; Allcca, A. E. L.; Shen, K.; Taniguchi, T.; Watanabe, K.; Bhave, S. A.; Chen, Y. P.; Ping, Y.; Li, T. Nuclear Spin Polarization and Control in Hexagonal Boron Nitride. *Nat. Mater.* **2022**, *21* (9), 1024–1028.
- (36) Gottscholl, A.; Kianinia, M.; Soltamov, V.; Orlinskii, S.; Mamin, G.; Bradac, C.; Kasper, C.; Krambrock, K.; Sperlich, A.; Toth, M.; Aharonovich, I.; Dyakonov, V. Initialization and Read-out of Intrinsic Spin Defects in a van Der Waals Crystal at Room Temperature. *Nat. Mater.* **2020**, *19* (5), 540–545.
- (37) Gao, X.; Jiang, B.; Llacsahuanga Allcca, A. E.; Shen, K.; Sadi, M. A.; Solanki, A. B.; Ju, P.; Xu, Z.; Upadhyaya, P.; Chen, Y. P.; Bhave, S. A.; Li, T. High-Contrast Plasmonic-Enhanced Shallow Spin Defects in Hexagonal Boron Nitride for Quantum Sensing. *Nano Lett.* **2021**, *21* (18), 7708–7714.
- (38) Koenderink, A. F. Single-Photon Nanoantennas. *ACS Photonics* **2017**, *4* (4), 710–722.
- (39) Pelton, M. Modified Spontaneous Emission in Nanophotonic Structures. *Nat. Photonics* **2015**, *9* (7), 427–435.
- (40) Tame, M. S.; McEnergy, K. R.; Özdemir, S. K.; Lee, J.; Maier, S. A.; Kim, M. S. Quantum Plasmonics. *Nat. Phys.* **2013**, *9* (6), 329–340.
- (41) Mendelson, N.; Ritika, R.; Kianinia, M.; Scott, J.; Kim, S.; Fröch, J. E.; Gazzana, C.; Westerhausen, M.; Xiao, L.; Mohajerani, S. S.; Strauf, S.; Toth, M.; Aharonovich, I.; Xu, Z. Q. Coupling Spin Defects in a Layered Material to Nanoscale Plasmonic Cavities. *Adv. Mater.* **2022**, *34* (1), 2106046.
- (42) Bogdanov, S. I.; Boltasseva, A.; Shalaev, V. M. Overcoming Quantum Decoherence with Plasmonics. *Science* **2019**, *364* (6440), S32–S33.
- (43) Rodionov, I. A.; Baburin, A. S.; Gabidullin, A. R.; Maklakov, S. S.; Peters, S.; Ryzhikov, I. A.; Andriyash, A. V. Quantum Engineering

of Atomically Smooth Single-Crystalline Silver Films. *Sci. Rep.* **2019**, 9, 12232.

(44) Rodionov, I. A.; Baburin, A. S.; Ryzhikov, I. A. Single-Crystalline Metal Films. US Patent App. 16/958,825, 2021.

(45) Bogdanov, S. I.; Shalaginov, M. Y.; Lagutchev, A. S.; Chiang, C. C.; Shah, D.; Baburin, A. S.; Ryzhikov, I. A.; Rodionov, I. A.; Kildishev, A. V.; Boltasseva, A.; Shalaev, V. M. Ultrabright Room-Temperature Sub-Nanosecond Emission from Single Nitrogen-Vacancy Centers Coupled to Nanopatch Antennas. *Nano Lett.* **2018**, 18 (8), 4837–4844.

(46) Bogdanov, S. I.; Makarova, O. A.; Xu, X.; Martin, Z. O.; Lagutchev, A. S.; Olinde, M.; Shah, D.; Chowdhury, S. N.; Gabidullin, A. R.; Ryzhikov, I. A.; Rodionov, I. A.; Kildishev, A. V.; Bozhevolnyi, S. I.; Boltasseva, A.; Shalaev, V. M.; Khurgin, J. B. Ultrafast Quantum Photonics Enabled by Coupling Plasmonic Nanocavities to Strongly Radiative Antennas. *Optica* **2020**, 7 (5), 463–469.

(47) Fröch, J. E.; Spencer, L. P.; Kianinia, M.; Totonjian, D. D.; Nguyen, M.; Gottscholl, A.; Dyakonov, V.; Toth, M.; Kim, S.; Aharonovich, I. Coupling Spin Defects in Hexagonal Boron Nitride to Monolithic Bullseye Cavities. *Nano Lett.* **2021**, 21 (15), 6549–6555.

(48) Baburin, A. S.; Merzlikin, A. M.; Baryshev, A. V.; Ryzhikov, I. A.; Panfilov, Y. V.; Rodionov, I. A. Silver-Based Plasmonics: Golden Material Platform and Application Challenges [Invited]. *Opt. Mater. Express* **2019**, 9 (2), 611–642.

(49) Park, J. H.; Ambwani, P.; Manno, M.; Lindquist, N. C.; Nagpal, P.; Oh, S. H.; Leighton, C.; Norris, D. J. Single-Crystalline Silver Films for Plasmonics. *Adv. Mater.* **2012**, 24 (29), 3988–3992.

(50) Wu, Y.; Zhang, C.; Estakhri, N. M.; Zhao, Y.; Kim, J.; Zhang, M.; Liu, X. X.; Pribil, G. K.; Alù, A.; Shih, C. K.; Li, X. Intrinsic Optical Properties and Enhanced Plasmonic Response of Epitaxial Silver. *Adv. Mater.* **2014**, 26 (35), 6106–6110.

(51) Kishida, H.; Mikkelsen, M. H. Ultrafast Lifetime and Bright Emission from Graphene Quantum Dots Using Plasmonic Nanogap Cavities. *Nano Lett.* **2022**, 22 (3), 904–910.

(52) Akselrod, G. M.; Argyropoulos, C.; Hoang, T. B.; Ciraci, C.; Fang, C.; Huang, J.; Smith, D. R.; Mikkelsen, M. H. Probing the Mechanisms of Large Purcell Enhancement in Plasmonic Nanantennas. *Nat. Photonics* **2014**, 8 (11), 835–840.

(53) Faggiani, R.; Yang, J.; Lalanne, P. Quenching, Plasmonic, and Radiative Decays in Nanogap Emitting Devices. *ACS Photonics* **2015**, 2 (12), 1739–1744.

(54) Fehler, K. G.; Antoniuk, L.; Lettner, N.; Ovyyan, A. P.; Waltrich, R.; Gruhler, N.; Davydov, V. A.; Agafonov, V. N.; Pernice, W. H. P.; Kubanek, A. Hybrid Quantum Photonics Based on Artificial Atoms Placed Inside One Hole of a Photonic Crystal Cavity. *ACS Photonics* **2021**, 8 (9), 2635–2641.

(55) Bogdanov, S. I.; Makarova, O. A.; Lagutchev, A. S.; Shah, D.; Chiang, C.-C.; Saha, S.; Baburin, A. S.; Ryzhikov, I. A.; Rodionov, I. A.; Kildishev, A. V.; Boltasseva, A.; Shalaev, V. M. Deterministic Integration of Single Nitrogen-Vacancy Centers into Nanopatch Antennas. *arXiv (Quantum Physics)*, February 15, 2019, <https://arxiv.org/abs/1902.05996>.

(56) Dréau, A.; Lesik, M.; Rondin, L.; Spinicelli, P.; Arcizet, O.; Roch, J. F.; Jacques, V. Avoiding Power Broadening in Optically Detected Magnetic Resonance of Single NV Defects for Enhanced DC Magnetic Field Sensitivity. *Phys. Rev. B - Condens. Matter Mater. Phys.* **2011**, 84 (19), 195204.

(57) Solanki, A. B.; Bogdanov, S. I.; Rahman, M. M.; Rustagi, A.; Dilley, N. R.; Shen, T.; Tong, W.; Debashis, P.; Chen, Z.; Appenzeller, J.; Chen, Y. P.; Shalaev, V. M.; Upadhyaya, P. Electric Field Control of Interaction between Magnons and Quantum Spin Defects. *Phys. Rev. Res.* **2022**, 4 (1), L012025.

## □ Recommended by ACS

### Quantum Emitters in Hexagonal Boron Nitride

Igor Aharonovich, Milos Toth, et al.

NOVEMBER 22, 2022

NANO LETTERS

READ ▶

### Site-Specific Fabrication of Blue Quantum Emitters in Hexagonal Boron Nitride

Angus Gale, Milos Toth, et al.

MAY 18, 2022

ACS PHOTONICS

READ ▶

### Defect Engineering of Monoisotopic Hexagonal Boron Nitride Crystals via Neutron Transmutation Doping

Jiahua Li, James H. Edgar, et al.

NOVEMBER 18, 2021

CHEMISTRY OF MATERIALS

READ ▶

### Large-Scale, High-Yield Laser Fabrication of Bright and Pure Single-Photon Emitters at Room Temperature in Hexagonal Boron Nitride

Lin Gan, Cun-Zheng Ning, et al.

AUGUST 18, 2022

ACS NANO

READ ▶

Get More Suggestions >